Supplement of Atmos. Chem. Phys., 22, 10955–10970, 2022
https://doi.org/10.5194/acp-22-10955-2022-supplement

Supplement of

A comprehensive study on hygroscopic behaviour and nitrate depletion of $NaNO_3$ and dicarboxylic acid mixtures: implications for nitrate depletion in tropospheric aerosols

Shuaishuai Ma et al.

Correspondence to: Shuaishuai Ma (mass@qzc.edu.cn) and Yunhong Zhang (yhz@bit.edu.cn)

Hygroscopic behaviour and IR features of individual components

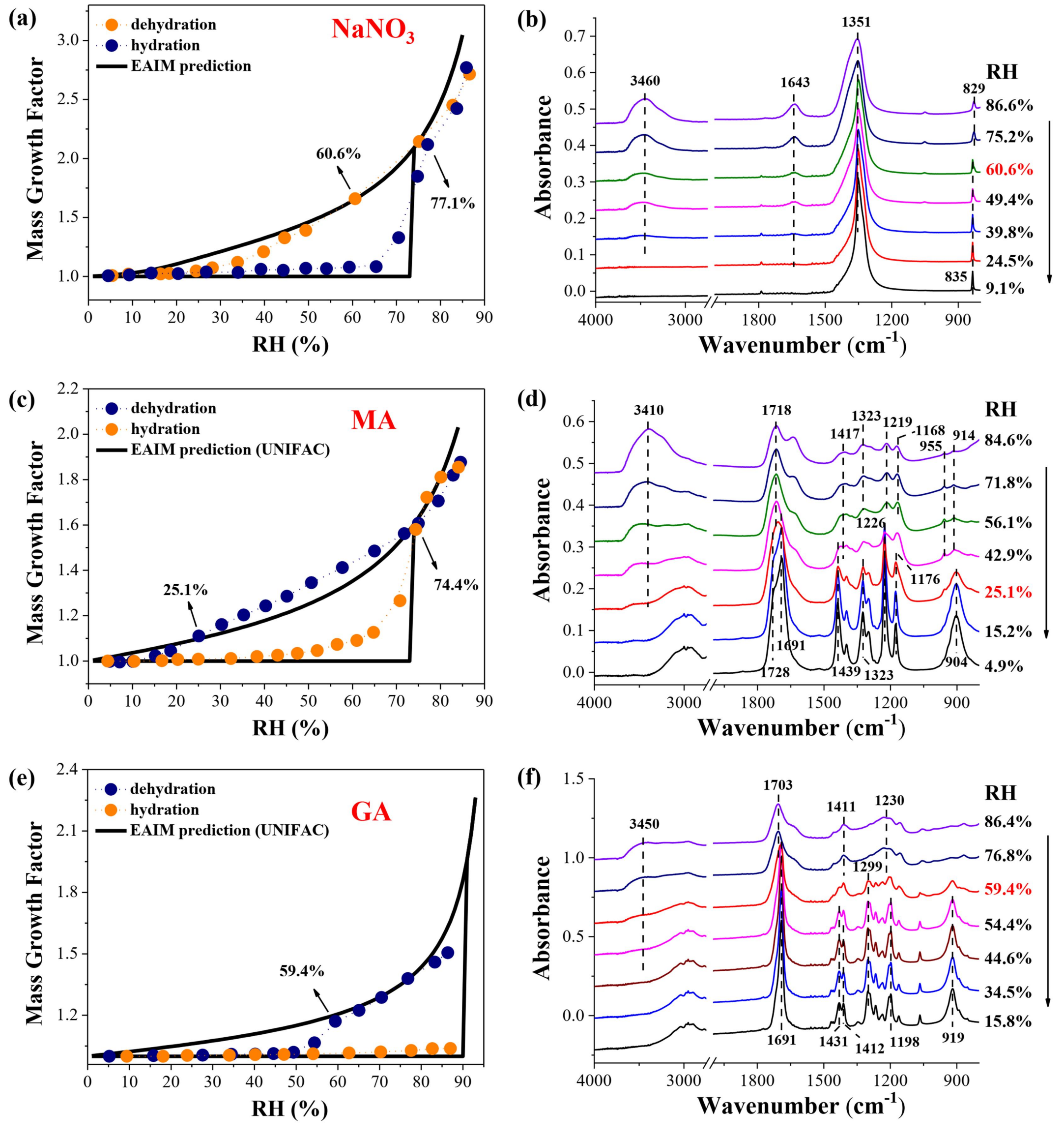

Figure S1. Hygroscopic growth curves during a RH cycle for pure $NaNO_3$ (a), MA (c), and GA (e) particles measured by ATR-FTIR and the comparison with EAIM predictions, as well as the IR spectra of pure $NaNO_3$ (b), MA (d), and GA (f) particles upon dehydration.

The hygroscopic growth curves of pure $NaNO_3$, MA, and GA particles measured by ATR-FTIR are shown in Fig. S1a, S1c, and S1e, respectively. Corresponding IR spectra during the dehumidification are shown in Fig. S1b, S1d, and S1f, respectively. For $NaNO_3$ particles, the measured initial ERH is ~ 60.6%, considerably consistent with the measurement value of 62.5% ERH from Zhang et al. (2014). Meanwhile, the 1351 cm^{-1} band assigned to $v_3(NO_3^-)$ becomes sharper, and the out-of-plane deformation $v_2(NO_3^-)$ located at 829 cm^{-1} red-shifts to 835 cm^{-1}, indicating the $NaNO_3$ solids formation (Zhang et al., 2014; Liu et al., 2008). Furthermore, the hygroscopic growth and IR spectra of deposited $NaNO_3$ particles on CaF_2 substrates are measured by vacuum FTIR method, as shown in Fig. S2. The 1350 cm^{-1} band assigned to $v_3(NO_3^-)$ also becomes sharper upon drying. More importantly, the $v_3(NO_3^-)$ feature bands in the two measurements are inconsistent with the IR feature of $NaNO_3$ crystals, i.e., two shoulder peaks centred at 1383 and 1485 cm^{-1} arising from splitting of the degenerate v_3 mode (Liu et al., 2008). This implies that non-crystalline particle morphology is formed after drying. In addition, Liu et al. (2008) also found small amounts of water present within particles after dehydration and the particles absorb water continuously upon hydration, potentially indicating the formation of highly concentrated droplets after drying. In the present study, the 1640 cm^{-1} band is barely visible after dehydration, and effloresced $NaNO_3$ particles do not absorb water until the DRH. Likewise, Tang and Fung (1997) observed that the Raman spectra characteristic of dried $Sr(NO_3)_2$ and $Ca(NO_3)_2$ particles was obviously different from that of anhydrous crystals, indicative of amorphous solids formation. Meanwhile, no sharp decrease in the water content of $Ca(NO_3)_2$ particles was observed during the dehumidification, and the amorphous solids would deliquesce at RH well below the DRH of anhydrous crystals, which were in good agreement with the observations for

$NaNO_3$ particles in this work. Based on these, the formation of amorphous $NaNO_3$ solids after dehydration in the two measurements can be inferred here.

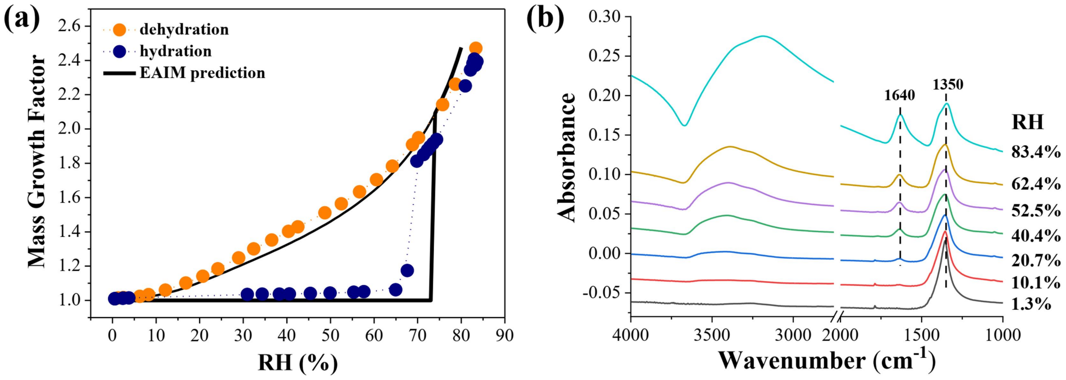

Figure S2. Hygroscopic growth curve of pure $NaNO_3$ particles (a) and corresponding IR spectra upon dehydration (b) measured by vacuum FTIR.

The OA droplets can be effloresced at RH as high as 90% induced by the Ge substrate, and OA crystals cannot be deliquesced due to the DRH higher than 90% (Ma et al., 2013; Wang et al., 2017). Thus, the water cycle curve of OA is not presented here, and only the IR spectra during the dehumidification are shown in Fig. S3. At RH > 90%, the 1744 cm^{-1} band is assigned to the stretching mode of C=O (v(C=O)) of liquid OA, and the 1355 cm^{-1} and 1233 cm^{-1} bands can be attributed to the bending mode of C-O-H (δ(C-O-H)) and the stretching mode of C-O (v(C-O)), respectively (Stace and Oralratmanee, 1973; Redington and Redington, 1978). Then at ~ 60% RH, the shoulder peaks at 3441 and 3404 cm^{-1} are assigned to v(OH) of OA dihydrate, and the peak at 1680 cm^{-1} is attributed to v(C=O) of OA dihydrate, consistent with the reference spectrum from Chemistry WebBook of National Institute of Standards and Technology (NIST) of U.S.A. (blue curve in Fig. S3). As RH decreases to 10%, the 1680 cm^{-1} band becomes stronger and the 1744 cm^{-1} band becomes weaker, indicating the continuous transformation of liquid OA to OA dihydrate. A new sharp peak at 1722 cm^{-1} appears at ~ 5% RH, suggesting the crystalline water loss of OA dihydrate and the formation of anhydrous OA (Wang et al., 2019). This RH point agrees well with the measurement value from Wang et al. (2017). At ~ 3% RH, the OA dihydrate is consumed completely.

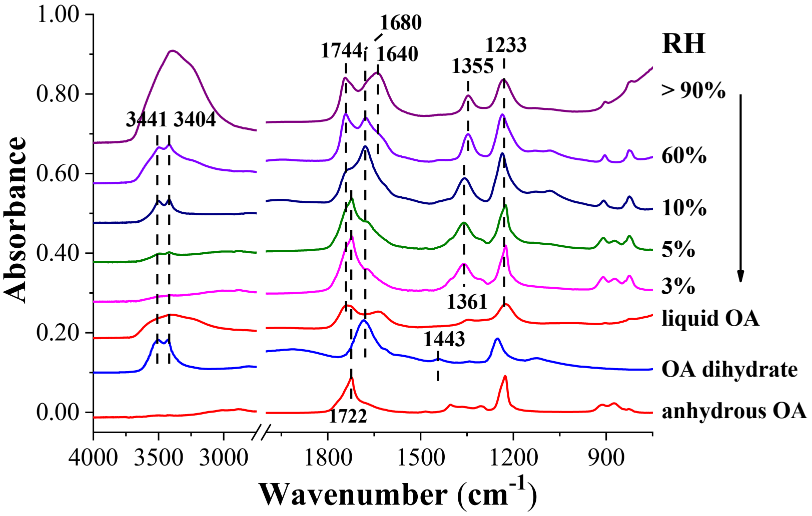

Figure S3. IR spectra of pure OA particles during the dehumidification measured by ATR-FTIR. Red curves represent the reference spectra of liquid and anhydrous OA from Wang et al. (2019). Blue curve indicates the reference spectrum of OA dihydrate from Chemistry WebBook of NIST of U.S.A.

For MA aerosols, the initial ERH is ~ 25.1% and the DRH is ~ 74.4%, comparable with the measurement values from Shao et al. (2018). As shown in Fig. S1d, the 1718 cm^{-1} band is assigned to *v*(C=O) of aqueous MA. After crystallization, the shoulder peaks at 1728 and 1691 cm^{-1} are characteristics of *v*(C=O) of crystalline MA, and the 1439 cm^{-1}, 1226 cm^{-1} and 1176 cm^{-1} bands are also assigned to IR features of MA solid phase (Shao et al., 2018). Pure GA particles deposited on Ge substrate tend to nucleate heterogeneously at ~ 59.4% RH, and cannot be deliquesced at RH up to ~ 86% due to the very high DRH of GA (Marcolli et al., 2004; Yeung et al., 2010; Peng et al., 2001; Pope et al., 2010). In Fig. S1f, the feature bands at 1691 cm^{-1}, 1299 cm^{-1}, 1198 cm^{-1} and 919 cm^{-1} are characteristics of crystalline GA solids (Ghorai et al., 2014; Cziczo et al., 1997; Wu et al., 2019).

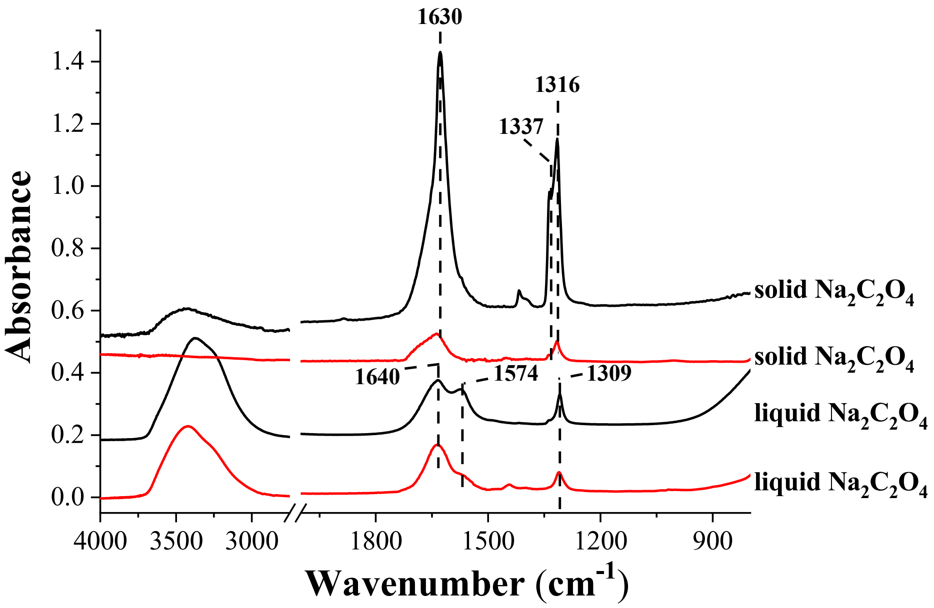

Figure S4. IR spectra of solid and liquid $Na_2C_2O_4$ particles measured by ATR-FTIR in this work (black curves) and from Wang et al. (2019) (red curves).

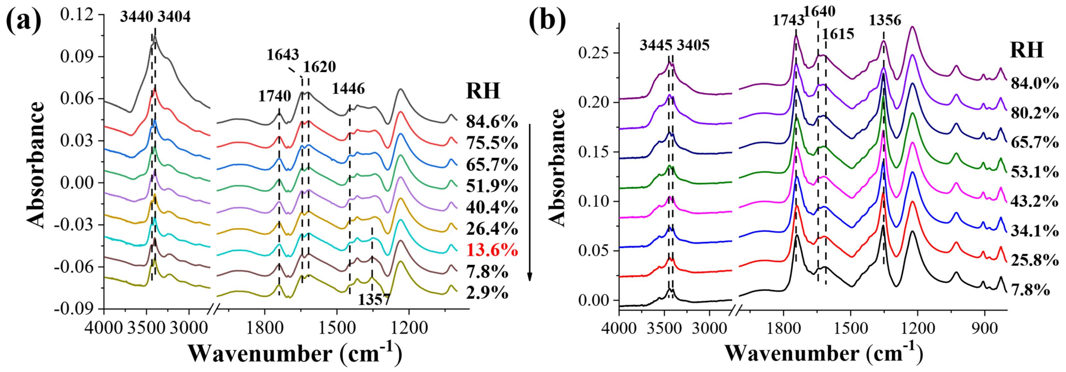

Figure S5. IR spectra of 1:1 mixed $NaNO_3$/OA particles during the dehumidification in vacuum FTIR measurement (a) and during the humidification in ATR-FTIR measurement (b).

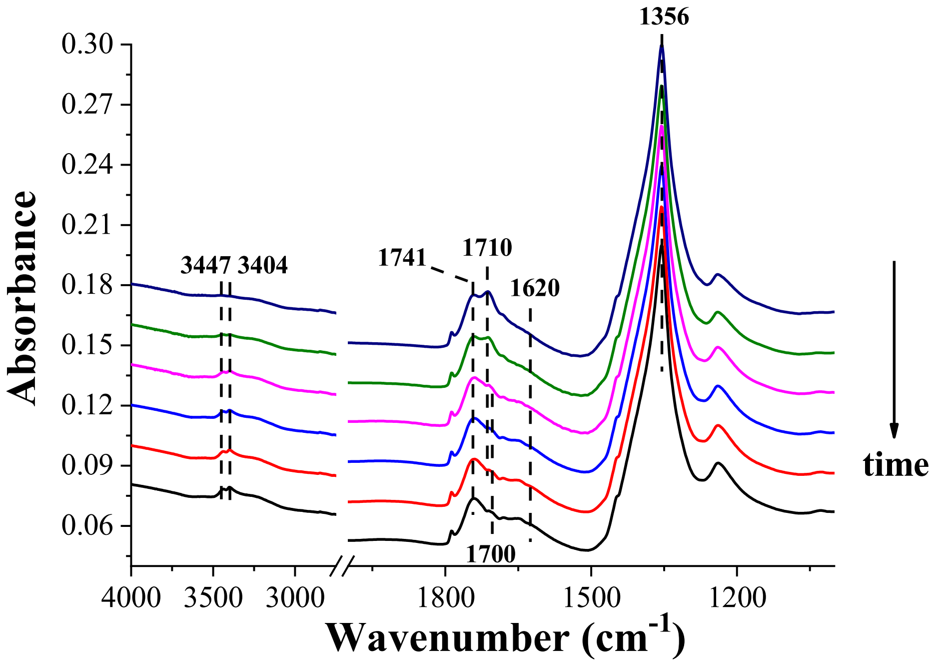

Figure S6. IR spectra changes of 3:1 $NaNO_3$/OA mixed particles at different time under constant ~ 15% RH.

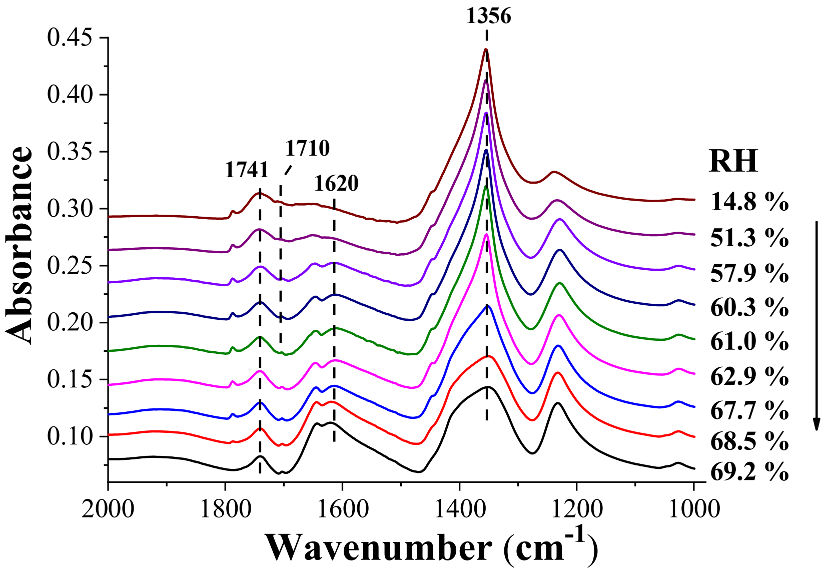

100

101 **Figure S7.** IR spectra changes of 3:1 $NaNO_3$/OA mixed particles during the shaded period in Fig.

102 3a.

103

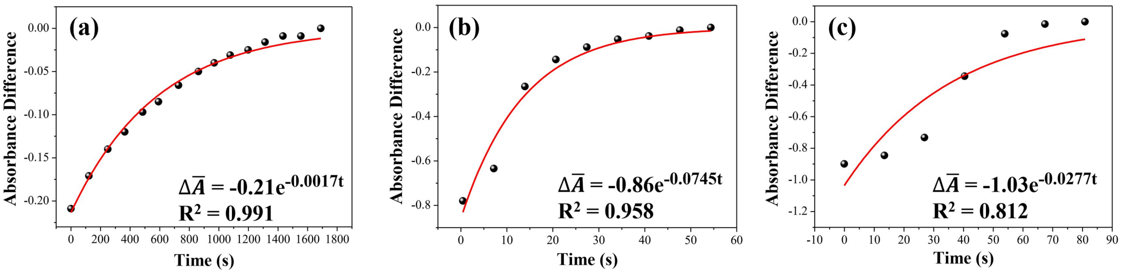

Figure S8. Changes in absorbance difference of $v_{\mathrm{as}}(\mathrm{COO}^-)$ band, $\Delta\bar{A}$, as a function of initialized reaction time in three RH ranges, i.e., constant ~ 15% (a), 14.8-61.0% (b), and 66.2-69.2% (c). The red curves indicate the exponential fitting of absorbance difference data.

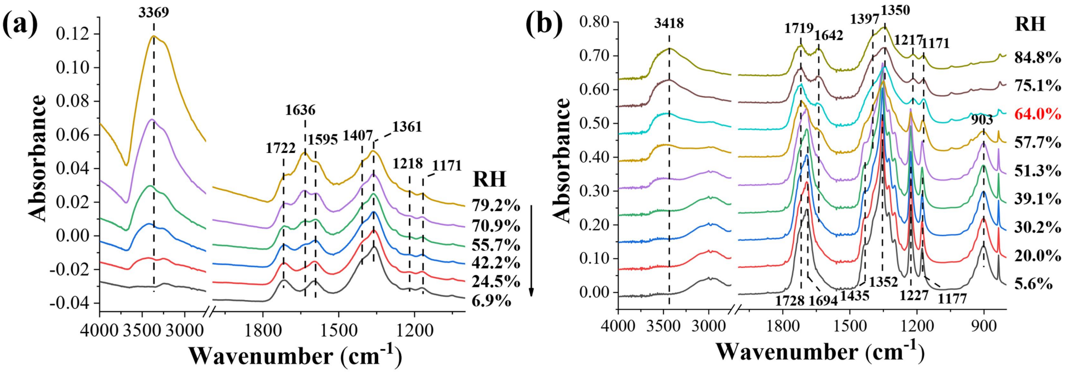

Figure S9. IR spectra of 1:1 mixed $NaNO_3$/MA particles during the dehumidification in vacuum FTIR measurement (a) and during the humidification in ATR-FTIR measurement (b).

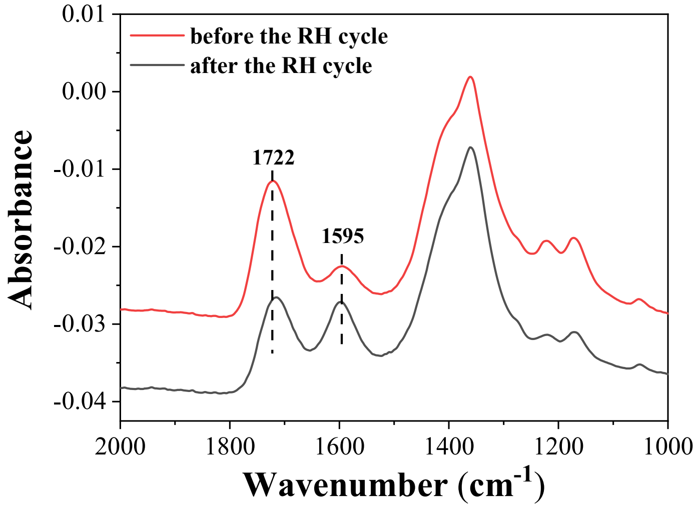

Figure S10. IR spectra of 1:1 $NaNO_3$/MA mixtures in the range of 2000-1000 cm^{-1} before and after the RH cycle.

Chemical reaction between internally mixed NaCl and MA

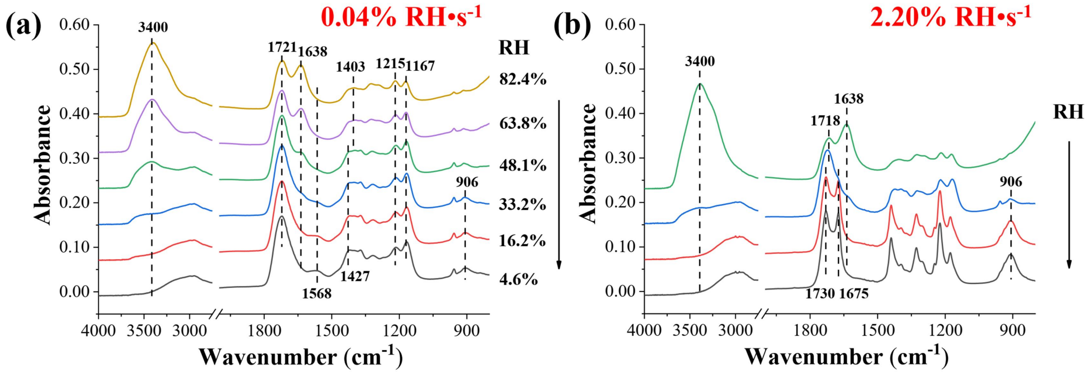

Figure S11. IR spectra of 1:1 mixed NaCl/MA particles during the dehumidification with two RH changing rates, i.e., 0.04% RH·s^{-1} (a) and 2.20% RH·s^{-1} (b), in ATR-FTIR measurements.

The chemical reaction between internally mixed NaCl and MA is explored by ATR-FTIR. Fig. S12a shows the IR spectra of 1:1 NaCl/MA mixtures during the dehumidification with the RH changing rate of 0.04% RH·s^{-1}. When the RH decreases from 82.4% to 4.6%, the red shift of feature band from 1403 cm^{-1} to 1427 cm^{-1} and the appearance of 906 cm^{-1} band illustrate the crystallization of MA (Shao et al., 2017). Nevertheless, the splitting of 1721 cm^{-1} band and the shift of feature bands at 1215 and 1167 cm^{-1}, which will occur during liquid-solid phase transition of MA, cannot be observed, potentially implying the partial crystallization of NaCl/MA mixtures. In Ghorai's study, the submicrometer NaCl/MA mixed particles with mole ratio of 1:1 deposited on Si_3N_4 windows did not effloresce upon dehydration (Ghorai et al., 2014). While in Li's work, the supermicrometer 1:1 NaCl/MA mixtures (~12-15 μm in diameter at RH = ~90%) deposited on Si substrate would effloresce at ~ 32.5% RH (Li et al., 2017). Furthermore, Ling and Chan (2008) also observed the partial crystallization of both $(NH_4)_2SO_4$ and MA for 1:1 mixed particle levitated in electrodynamic balance. These controversial results can be attributed to the substrate effect, particle size, or trace impurities contained in aqueous droplets (Ma et al., 2021). As RH decreases to ~ 33.2%, a new peak located at 1568 cm^{-1} assigned to $\nu_{as}(COO^{-})$ of $CH_2(COONa)_2$ appears, suggesting the formation of disodium malonate (Wang et al., 2019; Ma et al., 2013). The disodium salts production demonstrates greater chemical reactivity of NaCl than $NaNO_3$ with diacids due to stronger volatility of HCl than HNO_3, i.e., lower K_H value of HCl (< 2×10^{-1} M/atm) than that of HNO_3 (> 2×10^{5} M/atm) (Laskin et al., 2012). However, the experimental result is inconsistent with the observation by Ma et al. (2013), in which the chloride depletion in NaCl/MA mixtures would not occur in a speedy drying process. They explained that the rapid drying process minimized the HCl release from mixed droplets. Herein, the dehumidification process of NaCl/MA mixtures with a higher RH changing rate of 2.20% RH·s^{-1} is monitored by ATR-FTIR, as shown in Fig. S12b. It is obvious that no malonate sodium salts are formed upon drying. Meanwhile, the crystallization of mixtures can be clearly distinguished. This is because the high dehumidification rate will cause rapid water evaporation, which leads to lower temperature of droplets and further facilitates the crystallization of particles (Ma et al., 2019). There are two probable causes for no chloride depletion observed in the fast drying process. One is the minimization of HNO_3 release caused by rapid water evaporation. Another cause is the efflorescence transition of mixed particles at relatively high RH.

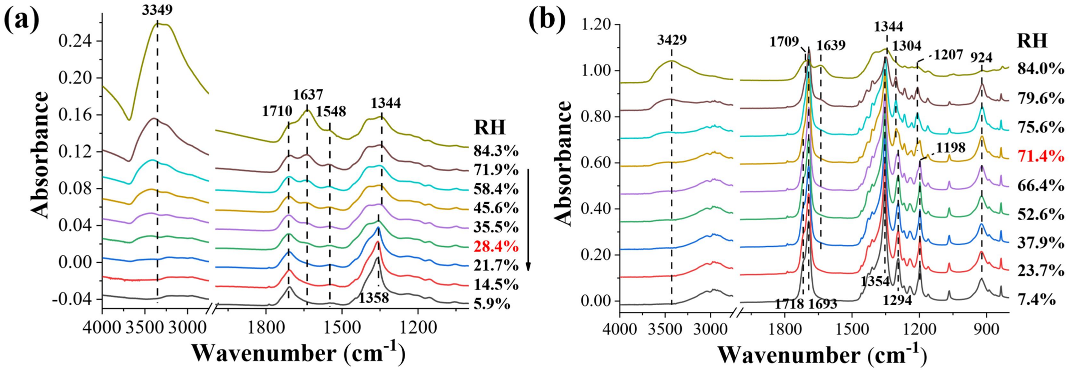

Figure S12. IR spectra of 1:1 mixed $NaNO_3$/GA particles during the dehumidification in vacuum FTIR measurement (a) and during the humidification in ATR-FTIR measurement (b).

Calculation method of the water activity a_w

The water activity a_w of aqueous droplets can be determined by Köhler equation:

$$a_w = \mathrm{RH} \cdot \exp\left(\frac{-4\sigma_\mathrm{sol} M_\mathrm{w}}{RT\ {}_\mathrm{w}D_\mathrm{p}}\right) \tag{1}$$

where σ_sol denotes the surface tension of aqueous droplets, which is suggested to be equal to that of pure water (0.072 J m^{-2}); M_w is the molecular weight of water (kg mol^{-1}); R is the ideal gas constant (J mol^{-1} K^{-1}); T is the temperature (K); ρ_w is the density of water (kg m^{-3}); D_p is the droplet diameter (m).

Simulation process for pH changes dependent upon nitrate depletion extent in $NaNO_3$/DCAs mixtures

Assuming that thermodynamic equilibrium is reached in 1:1 mixed $NaNO_3/H_2A$ (org) aqueous system with an initial concentration C_0 of 0.1 mol/L, two dissociation equilibriums for H_2A (org) can be established in solution:

$$\mathrm{H_2A} \overset{K_1}{\leftrightarrow} \mathrm{H^+} + \mathrm{HA^-}, \mathrm{HA^-} \overset{K_2}{\leftrightarrow} \mathrm{H^+} + \mathrm{A^{2-}}$$

The equilibrium concentration of HA^- and A^{2-}, denoted by $[HA^-]$ and $[A^{2-}]$ respectively, can be expressed as

$$[\mathrm{HA^-}] = \frac{K_1[\mathrm{H_2A}]}{[\mathrm{H^+}]} \tag{2}$$

$$[\mathrm{A^{2-}}] = \frac{K_2K_1[\mathrm{H_2A}]}{[\mathrm{H^+}]^2} \tag{3}$$

where $[H_2A]$ and $[H^+]$ represent the equilibrium concentration of H_2A and H^+ in solution, respectively; K_1 and K_2 are equal to the primary and secondary dissociation constant of H_2A, K_{a1} and K_{a2}, respectively. According to the material balance principle, the following equation can be derived:

$$\mathrm{C_0} = [\mathrm{H_2A}] + [\mathrm{HA^-}] + [\mathrm{A^{2-}}] \tag{4}$$

Combining the eq. (2) and (3), the eq. (4) can be rewritten as

$$\mathrm{C_0} = \frac{K_1[\mathrm{H^+}]+[\mathrm{H^+}]^2+K_2K_1}{[\mathrm{H^+}]^2} \cdot [\mathrm{H_2A}] \tag{5}$$

Thus, the $[HA^-]$ and $[A^{2-}]$ can be expressed as

$$[\mathrm{HA^-}] = \frac{K_1C_0[\mathrm{H^+}]}{K_1[\mathrm{H^+}]+[\mathrm{H^+}]^2+K_2K_1} \tag{6}$$

$$[\mathrm{A^{2-}}] = \frac{K_2K_1C_0}{K_1[\mathrm{H^+}]+[\mathrm{H^+}]^2+K_2K_1} \tag{7}$$

Moreover, another balance between NO_3^- and HNO_3 (aq) is present in solution:

$$\mathrm{H^+} + \mathrm{NO_3}^- \overset{K_3}{\leftrightarrow} \mathrm{HNO_3}$$

where K_3 is the inverse of the acid dissociation constant of HNO_3. The equilibrium concentration of NO_3^- and HNO_3 (aq), $[NO_3^-]$ and $[HNO_3]$, can be associated as

$$[\mathrm{HNO_3}] = K_3[\mathrm{H^+}][\mathrm{NO_3^-}] \tag{8}$$

The concentration of depleted NO_3^-, i.e., formed gaseous HNO_3, is denoted as C_1, and then the following equation can be derived according to mass balance principle:

$$\mathrm{C_0} = [\mathrm{NO_3^-}] + [\mathrm{HNO_3}] + \mathrm{C_1} \tag{9}$$

Thus, the $[HNO_3]$ can be rewritten by combining eq. (8) and (9):

$$[\mathrm{HNO_3}] = \frac{K_3[\mathrm{H^+}](C_0-C_1)}{K_3[\mathrm{H^+}]+1} \tag{10}$$

On the basis of the H^+ ion conservation, the following equation can be derived:

$$[\mathrm{H^+}] = [\mathrm{H_3O^+}] + [\mathrm{HA^-}] + 2[\mathrm{A^{2-}}] - [\mathrm{HNO_3}] - \mathrm{C_1} \tag{11}$$

Then, the relation between C_1 and $[H^+]$ can be determined by combining eq. (6), (7) and (10) into eq. (11):

$$\mathrm{C_1} = (K_3[\mathrm{H^+}]+1)\cdot\left(\frac{K_w}{[\mathrm{H^+}]} + \frac{K_1C_0[\mathrm{H^+}]+2K_2K_1C_0}{K_1[\mathrm{H^+}]+[\mathrm{H^+}]^2+K_2K_1} - [\mathrm{H^+}] - \frac{K_3C_0[\mathrm{H^+}]}{K_3[\mathrm{H^+}]+1}\right) \tag{12}$$

The K_1, K_2 and K_3 values for different acids are listed in Table 2 in the text. Thus, the C_1 values can be determined with changing $[H^+]$, i.e., the different droplet pH according to pH = $-\log_{10}$ $[H^+]$. Note that the defined pH here is a free-H^+ approximation of pH on a molality basis, as indicated by Pye et al. (2020). The nitrate depletion fraction is determined by the ratio of depleted $[NO_3^-]$ (C_1) to the initial concentration of NO_3^- (C_0 = 0.1 mol/L).

References

Cziczo, D. J., Nowak, J. B., Hu, J. H., and Abbatt, J. P. D.: Infrared spectroscopy of model tropospheric aerosols as a function of relative humidity: Observation of deliquescence and crystallization, J. Geophys. Res., 102, 18843-18850, https://doi.org/10.1029/97jd01361, 1997.

Ghorai, S., Wang, B. B., Tivanski, A., and Laskin, A.: Hygroscopic properties of internally mixed particles composed of NaCl and water-soluble organic acids, Environ. Sci. Technol., 48, 2234-2241, https://doi.org/10.1021/es404727u, 2014.

Laskin, A., Moffet, R. C., Gilles, M. K., Fast, J. D., Zaveri, R. A., Wang, B. B., Nigge, P., and Shutthanandan, J.: Tropospheric chemistry of internally mixed sea salt and organic particles: Surprising reactivity of NaCl with weak organic acids, J. Geophys. Res.-Atmos., 117, D15302, https://doi.org/10.1029/2012jd017743, 2012.

Li, X., Gupta, D., Lee, J., Park, G., and Ro, C.-U.: Real-time investigation of chemical compositions and hygroscopic properties of aerosols generated from NaCl and malonic acid mixture solutions using in situ Raman microspectrometry, Environ. Sci. Technol., 51, 263-270, https://doi.org/10.1021/acs.est.6b04356, 2017.

Ling, T. Y., and Chan, C. K.: Partial crystallization and deliquescence of particles containing ammonium sulfate and dicarboxylic acids, J. Geophys. Res.-Atmos., 113, D14205, https://doi.org/10.1029/2008jd009779, 2008.

Liu, Y., Yang, Z. W., Desyaterik, Y., Gassman, P. L., Wang, H., and Laskin, A.: Hygroscopic behavior of substrate-deposited particles studied by micro-FT-IR spectroscopy and complementary methods of particle analysis, Anal. Chem., 80, 633-642, https://doi.org/10.1021/ac701638r, 2008.

Ma, Q. X., Ma, J. Z., Liu, C., Lai, C. Y., and He, H.: Laboratory study on the hygroscopic behavior of external and internal C_2–C_4 dicarboxylic acid–NaCl mixtures, Environ. Sci. Technol., 47, 10381-10388, https://doi.org/10.1021/es4023267, 2013.

Ma, S. S., Yang, W., Zheng, C. M., Pang, S. F., and Zhang, Y. H.: Subsecond measurements on aerosols: From hygroscopic growth factors to efflorescence kinetics, Atmos. Environ., 210, 177-185, https://doi.org/10.1016/j.atmosenv.2019.04.049, 2019.

Ma, S. S., Pang, S. F., Li, J., and Zhang, Y. H.: A review of efflorescence kinetics studies on atmospherically relevant particles, Chemosphere, 277, 130320, https://doi.org/10.1016/j.chemosphere.2021.130320, 2021.

Marcolli, C., Luo, B., and Peter, T.: Mixing of the organic aerosol fractions: Liquids as the thermodynamically stable phases, J. Phys. Chem. A, 108, 2216-2224, https://doi.org/10.1021/jp036080l, 2004.

Peng, C. G., Chan, M. N., and Chan, C. K.: The hygroscopic properties of dicarboxylic and multifunctional acids: Measurements and UNIFAC predictions, Environ. Sci. Technol., 35, 4495-4501, https://doi.org/10.1021/es0107531, 2001.

Pope, F. D., Dennis-Smither, B. J., Griffiths, P. T., Clegg, S. L., and Cox, R. A.: Studies of single aerosol particles containing malonic acid, glutaric acid, and their mixtures with sodium chloride. I. Hygroscopic growth, J. Phys. Chem. A, 114, 5335-5341, https://doi.org/10.1021/jp100059k, 2010.

Pye, H. O. T., Nenes, A., Alexander, B., Ault, A. P., Barth, M. C., Clegg, S. L., Collett Jr, J. L., Fahey, K. M., Hennigan, C. J., Herrmann, H., Kanakidou, M., Kelly, J. T., Ku, I. T., McNeill, V. F., Riemer, N., Schaefer, T., Shi, G., Tilgner, A., Walker, J. T., Wang, T., Weber, R., Xing, J., Zaveri, R. A., and Zuend, A.: The acidity of atmospheric particles and clouds, Atmos. Chem. Phys., 20, 4809-4888, https://doi.org/10.5194/acp-20-4809-2020, 2020.

Redington, R. L., and Redington, T. E.: Infrared matrix-isolation spectra of monomeric oxalic acid, J. Mol. Struct., 48, 165-176, https://doi.org/10.1016/0022-2860(78)80019-2, 1978.

Shao, X., Zhang, Y., Pang, S. F., and Zhang, Y. H.: Vacuum FTIR observation on hygroscopic properties and phase transition of malonic acid aerosols, Chem. Phys., 483-484, 7-11, https://doi.org/10.1016/j.chemphys.2016.11.001, 2017.

Shao, X., Wu, F. M., Yang, H., Pang, S. F., and Zhang, Y. H.: Observing HNO_3 release dependent upon metal complexes in malonic acid/nitrate droplets, Spectrochim. Acta A, 201, 399-404, https://doi.org/10.1016/j.saa.2018.05.026, 2018.

Stace, B. C., and Oralratmanee, C.: Infrared and Raman spectra of gaseous oxalic acid, J. Mol. Struct., 18, 339-342, https://doi.org/10.1016/0022-2860(73)85238-X, 1973.

Tang, I. N., and Fung, K. H.: Hydration and Raman scattering studies of levitated microparticles: $Ba(NO_3)_2$, $Sr(NO_3)_2$, and $Ca(NO_3)_2$, J. Chem. Phys., 106, 1653-1660, https://doi.org/10.1063/1.473318, 1997.

Wang, N., Jing, B., Wang, P., Wang, Z., Li, J. R., Pang, S. F., Zhang, Y. H., and Ge, M. F.: Hygroscopicity and compositional evolution of atmospheric aerosols containing water-soluble carboxylic acid salts and ammonium sulfate: Influence of ammonium depletion, Environ. Sci. Technol., 53, 6225-6234, https://doi.org/10.1021/acs.est.8b07052, 2019.

Wang, X. W., Jing, B., Tan, F., Ma, J. B., Zhang, Y. H., and Ge, M. F.: Hygroscopic behavior and chemical composition evolution of internally mixed aerosols composed of oxalic acid and ammonium sulfate, Atmos. Chem. Phys., 17, 12797-12812, https://doi.org/10.5194/acp-17-12797-2017, 2017.

Wu, F. M., Wang, N., Pang, S. F., and Zhang, Y. H.: Hygroscopic behavior and fractional crystallization of mixed $(NH_4)_2SO_4$/glutaric acid aerosols by vacuum FTIR, Spectrochim. Acta A, 208, 255-261, https://doi.org/10.1016/j.saa.2018.10.010, 2019.

Yeung, M. C., Ling, T. Y., and Chan, C. K.: Effects of the polymorphic transformation of glutaric acid particles on their deliquescence and hygroscopic properties, J. Phys. Chem. A, 114, 898-903, https://doi.org/10.1021/jp908250v, 2010.

Zhang, Q. N., Zhang, Y., Cai, C., Guo, Y. C., Reid, J. P., and Zhang, Y. H.: In situ observation on the dynamic process of evaporation and crystallization of sodium nitrate droplets on a ZnSe substrate by FTIR-ATR, J. Phys. Chem. A, 118, 2728-2737, https://doi.org/10.1021/jp412073c, 2014.